Universiteit
Leiden
The Netherlands

Multiwavelength study of dark globule DC 314.8-5.1: point-source identification and diffuse emission characterization

Kosmaczewski, E.; Stawarz, Ł.; Cheung, C.C.; Bamba, A.; Karska, A.; Monteiro Rocha, W.R.

Citation
Kosmaczewski, E., Stawarz, Ł., Cheung, C. C., Bamba, A., Karska, A., & Monteiro Rocha, W. R. (2023). Multiwavelength study of dark globule DC 314.8-5.1: point-source identification and diffuse emission characterization. *The Astrophysical Journal, 959*(1). doi:10.3847/1538-4357/ad077a

Version:	Publisher's Version
License:	Creative Commons CC BY 4.0 license
Downloaded from:	https://hdl.handle.net/1887/3718952

Note: To cite this publication please use the final published version (if applicable).

The Astrophysical Journal, 959:37 (14pp), 2023 December 10 https://doi.org/10.3847/1538-4357/ad077a
© 2023. The Author(s). Published by the American Astronomical Society.
OPEN ACCESS

Multiwavelength Study of Dark Globule DC 314.8–5.1: Point-source Identification and Diffuse Emission Characterization

E. Kosmaczewski[1], Ł Stawarz[1], C. C. Cheung[2], A. Bamba[3,4,5], A. Karska[6,7], and W. R. M. Rocha[8]
[1] Astronomical Observatory of the Jagiellonian University, ul. Orla 171, 30-244 Kraków, Poland; e.kosmaczewski@oa.uj.edu.pl
[2] Naval Research Laboratory, Space Science Division, Washington, DC 20375, USA
[3] Department of Physics, Graduate School of Science, The University of Tokyo, 7-3-1 Hongo, Bunkyo-ku, Tokyo 113-0033, Japan
[4] Research Center for the Early Universe, School of Science, The University of Tokyo, 7-3-1 Hongo, Bunkyo-ku, Tokyo 113-0033, Japan
[5] Trans-Scale Quantum Science Institute, The University of Tokyo, Tokyo 113-0033, Japan
[6] Max-Planck-Institut für Radioastronomie, Auf dem Hügel 69, D-53121, Bonn, Germany
[7] Institute of Astronomy, Faculty of Physics, Astronomy and Informatics, Nicolaus Copernicus University, ul. Grudziadzka 5, 87-100 Toruń, Poland
[8] Laboratory for Astrophysics, Leiden Observatory, Leiden University, P.O. Box 9513, NL 2300 RA Leiden, The Netherlands
Received 2022 September 6; revised 2023 October 23; accepted 2023 October 25; published 2023 December 4

Abstract

We present an analysis of multiwavelength observations of the dark globule DC 314.8–5.1, using data from the Gaia optical, Two Micron All Star Survey near-infrared, and Wide-field Infrared Survey Explorer mid-infrared surveys, dedicated imaging with the Spitzer Space Telescope, and X-ray data obtained with the Swift X-Ray Telescope (XRT). The main goal was to identify possible pre-main-sequence stars (PMSs) and young stellar objects (YSOs) associated with the globule. For this, we studied the infrared colors of all point sources within the boundaries of the cloud. After removing sources with nonstellar spectra, we investigated the Gaia parallaxes for the YSO candidates and found that none are physically related to DC 314.8–5.1. In addition, we searched for X-ray emission from PMSs with Swift-XRT, and found no 0.5–10 keV emission down to a luminosity level $\lesssim 10^{31}$ erg s^{-1}, typical of a PMS with mass $\geqslant 2\ M_{\odot}$. Our detailed inspection therefore supports a very young, "prestellar core" evolutionary stage for the cloud. Based on archival Planck and IRAS data, we moreover identify the presence of hot dust, with temperatures $\gtrsim$100 K, in addition to the dominant dust component at 14 K, originating with the associated reflection nebula.

Unified Astronomy Thesaurus concepts: Interstellar medium (847); Molecular clouds (1072); Young stellar objects (1834); Pre-main sequence stars (1290); Infrared astronomy (786); X-ray astronomy (1810)

1. Introduction

The physical state of molecular clouds at a given evolutionary stage is strongly dependent on the development of star formation within such systems (for a review see, e.g., Heyer & Dame 2015; Klessen & Glover 2016; Jørgensen et al. 2020). The interactions of young stellar objects (YSOs) with their host clouds are substantial in the early stages of star formation. Stars form when the dense cores of these clouds collapse, with the infall of material resulting in the gravitational potential energy heating the material and increasing its density up to $\sim 10^8$–10^9 cm^{-3} (Jørgensen et al. 2020). The main effects of star formation are the processing of the dust within the cloud, the disruption of the cloud structure, and the heating of the cloud material (Strom et al. 1975). These processes continue as the system is altered and disrupted by the evolving young star.

Consequently, there is much interest in studying clouds prior to the onset of star formation, in particular prestellar cores (see Bergin & Tafalla 2007 for a review). Much study has been done on the already known prestellar cores, TMC-1 and L134N, but a lot of this was restricted to the submillimeter and radio end of the electromagnetic spectrum (Bergin & Tafalla 2007). Kirk et al. (2005) did a survey for prestellar cores, detecting 29 cores with submillimeter observations, and established some basic characteristics expected of such prestellar cores, such as an average temperature of 10 K, volume densities of bright cores of 10^5–10^6 cm^{-3} and intermediate cores of 10^4–10^5 cm^{-3}, and additionally, they constrained the radial density profiles and lifetimes of such cores. The filamentary structure of molecular clouds down to the internal structures of dense cores was further studied by André et al. (2014).

It is with this context in mind that we examined the prestellar nature of the dark globule DC 314.8–5.1. Originally classified as a compact dark globule (Hartley et al. 1986), it has a serendipitous association with a field star that illuminates reflection from the cloud. Whittet (2007) concluded, from Infrared Astronomical Satellite (IRAS; Beichman et al. 1988) and Two Micron All Sky Survey (2MASS; Skrutskie et al. 2006) data, that the cloud is at the onset of low-mass star formation and further discussed the basic properties of the system. Whittet performed a 2MASS survey of an elliptical region with radii $7' \times 5'$ covering the extent of the cloud to identify potential YSOs, and found only two candidates out of the sample of 387 sources. One was excluded as an old star with significant dust reddening and the other remained a viable YSO candidate, hereafter referred to as "C1."

In Kosmaczewski et al. (2022), we showed the presence of divergent conditions for DC 314.8–5.1 as compared to molecular clouds with ongoing star formation. In particular, our study of the Spitzer Space Telescope Infrared Spectrograph (IRS; Houck et al. 2004) mid-infrared spectra revealed a surprisingly large cation-to-neutral ratio of polycyclic aromatic hydrocarbons (PAHs), which could be explained by lower-energy cosmic rays (CRs) ionizing the cloud's interior, in addition to photoionization by the star (see,

Original content from this work may be used under the terms of the Creative Commons Attribution 4.0 licence. Any further distribution of this work must maintain attribution to the author(s) and the title of the work, journal citation and DOI.

Table 1
Source Associations

Name	R.A. (J2000) [hh:mm:ss]	Decl. (J2000) [dd:mm:ss]	Gaia Parallax (mas)	Distance (pc)	Source Identification	Identification Method	Reference
(1)	(2)	(3)	(4)	(5)	(6)	(7)	(8)
DC 314.8–5.1	14:48:29.00	–65:15:54.00	⋯	⋯	Cloud center	Visual extinction map	Hartley et al. (1986)
HD 130079	14:49:16.55[a]	–65:15:18.72[a]	2.298 ± 0.019	$431.7^{+3.2}_{-4.3}$	B9V star	Spectral classification	Whittet (2007)
S	14:48:16.72	–65:21:45.60	⋯	⋯	Background galaxy	Color–color[b]	This work
2RXS	14:48:33.73	–65:17:38.90	⋯	⋯	Unknown	X-ray	This work; Boller et al. (2016)
TYC 9015-926-1	14:48:17.13	–65:12:33.05	2.167 ± 0.015	$456.6^{+3.1}_{-3.2}$	Background star	Photometric measurement	Høg et al. (2000)
C1	14:47:52.20	–65:16:01.00	0.073 ± 0.096	6670^{+3750}_{-2250}	Background star	SED[c]	This work; Whittet (2007)
C2	14:48:29.39	–65:14:48.52	2.262 ± 0.059	436^{+11}_{-11}	Class III/field star	SED[c]	This work
C3	14:49:07.96	–65:17:56.41	2.441 ± 0.310	442^{+75}_{-53}	Field star	SED[c]	This work

Note. Columns: (1) Object name; (2) R.A.; (3) decl.; (4) Gaia parallax; (5) distance from the Gaia parallax and reported by Bailer-Jones et al. (2021); (6) source identification; (7) identification method; (8) references for columns (6) and (7).
[a] R.A. and decl. for HD 130079 are based on the Swift UVOT data reported in this work.
[b] Source detected in this work by Swift-XRT and identified with the aid of WISE color–color diagrams.
[c] Sources selected in this work to have color–color cuts consistent with the spectral energy distribution (SED) of prestellar objects.

in this context, Bamba 2009). However, to confirm this, one must perform a deeper search, to rule out pre-/YSOs.

In this paper, we expand on YSO identification methods for this system, utilizing data from dedicated observations with Spitzer and the Neil Gehrels Swift Observatory (Swift; Burrows et al. 2000), as well as from archival Wide-field Infrared Survey Explorer (WISE; Wright et al. 2010), 2MASS, and Gaia (Gaia Collaboration et al. 2021) surveys. The main goals of the multiwavelength data analysis presented here are: (i) to identify YSO candidates utilizing infrared and optical imaging, (ii) to test for the presence of pre-main-sequence stars (PMSs) that exhibit no optical/infrared counterparts, and (iii) to characterize the diffuse emission seen at microwave and infrared frequencies.

2. Multiwavelength Overview

The DC 314.8–5.1 dark globule is located approximately 5° below the Galactic plane in the southern constellation Circinus (see Table 1). The B9 V field star HD 130079, located near the cloud's eastern boundary, illuminates a reflection nebula (Whittet 2007). The association of HD 130079 with DC 314.8–5.1 was established by van den Bergh & Herbst (1975), who identified the presence of the reflection nebula through a survey of southern globules with the Cerro Tololo Observatory. van den Bergh & Herbst (1975) further characterized the host cloud through absorption around the reflection nebulae, determined from the density of field stars. Later, Bourke et al. (1995b) used NH_3 observations to determine the physical characteristics (density, temperature, mass) of isolated dark clouds, including DC 314.8–5.1.

The parallax value for HD 130079 in Gaia Early Data Release 3 (EDR3; Gaia Collaboration et al. 2021) is 2.2981 ± 0.0194 mas. Bailer-Jones et al. (2021) used the Gaia data and additional analyses to estimate the distance to the star as $431.7^{+3.2}_{-4.3}$ pc. Using this value as the distance to the cloud, the cloud's $\sim 7' \times 5'$ radial angular dimensions translate to projected linear sizes of 0.9 pc × 0.6 pc, while the mean core number density of atomic hydrogen and the total cloud mass inferred from the extinction characteristics (see Whittet 2007) become $\sim 7 \times 10^3$ cm^{-3} and $\sim 160\ M_\odot$, respectively.

2.1. Planck

The left panel of Figure 1 presents the Planck map of the DC 314.8–5.1 region at 353 GHz; the Planck emission peak is offset by 1.′4 to the east from the nominal center of DC 314.8–5.1, per Table 1.

DC 314.8–5.1 is listed in the Planck Catalogue of Galactic Cold Clumps (PGCC; Planck Collaboration et al. 2016a) as PGCC G314.77–5.14. The Planck team created cold residual maps by subtracting a warm component from individual maps (at given frequencies) as described in Planck Collaboration et al. (2011). As such, cold sources will appear as positive departures, signifying lower temperatures than the surrounding background. The modeling of the cloud on the Planck 857 GHz cold residual map with an elliptical Gaussian returns FWHMs along the major and minor axes of $8.'36 \pm 0.'34$ and $4.'60 \pm 0.'19$, respectively. Through fitting a modified blackbody, $F_\nu \propto B_\nu(T) \times (\nu/\nu_0)^\beta$, to the Planck photometric band fluxes, a dust temperature of $T = 14 \pm 1$ K and spectral index $\beta = 1.8 \pm 0.2$ were derived.

The Planck Collaboration et al. (2016a) estimate of the distance to DC 314.8–5.1 from near-infrared extinction is 400 ± 370 pc. When combined with the Planck photometry, the resulting mass estimate and mean density for the cloud are $10 \pm 14\ M_\odot$ and 892 ± 544 cm^{-3}, respectively. For comparison, using the Gaia-measured distance, ∼432 pc, and considering only the error in the Planck flux measurement, we derive a mass of $12.0 \pm 0.8\ M_\odot$. Though somewhat unconstrained, these are both below the corresponding estimates by Hetem et al. (1988) and Whittet (2007) of 25 and $50\ M_\odot$, respectively.

2.2. IRAS

The Point Source Catalog for IRAS has angular resolutions of 0.′5, 0.′5, 1.′0, and 2.′0 for 12, 25, 60, and 100 μm, respectively. The catalog has completeness down to levels of 0.4, 0.5, 0.6, and 1.0 jansky (Jy) at 12, 25, 60, and 100 μm,

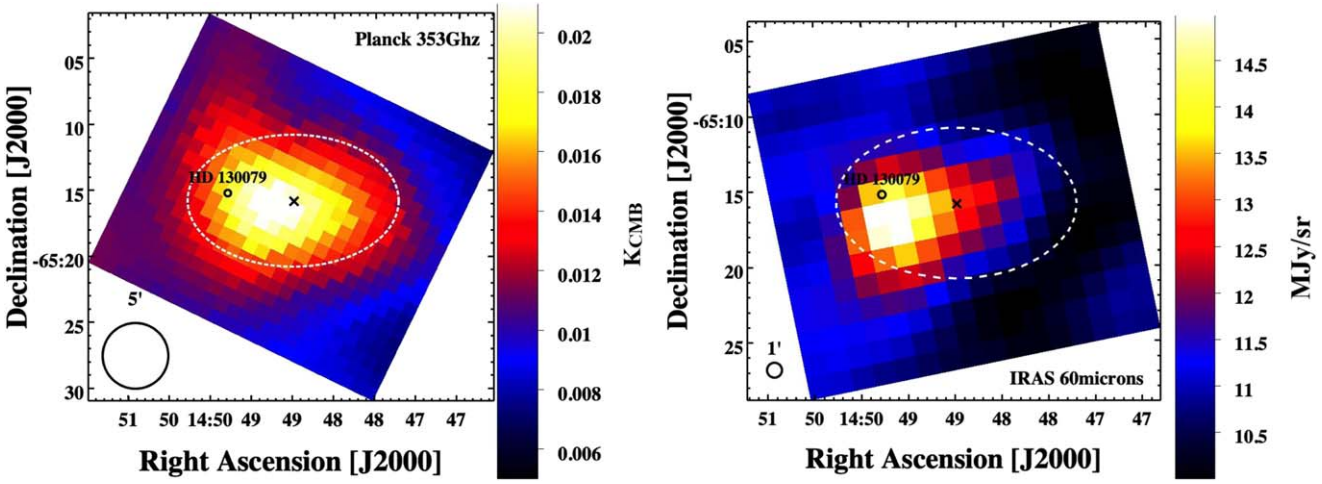

Figure 1. DC 314.8–5.1 as seen by Planck at 353 GHz (left panel) and IRAS at 60 μm (right panel). The white dashed ellipse (with radii of $\sim 7' \times 5'$) denotes the globule, with the central position marked by a black "×." The star HD 130079 is marked with a black open circle to the east of the cloud center.

respectively (Beichman et al. 1988). At the adopted distance of the cloud these correspond to monochromatic luminosities of 2.2×10^{33} erg s^{-1} ($\sim 0.58\ L_{\odot}$) at 12 μm, 1.3×10^{33} erg s^{-1} ($\sim 0.34\ L_{\odot}$) at 25 μm, and 6.7×10^{32} erg s^{-1} ($\sim 0.18\ L_{\odot}$) at 60 and 100 μm (Beichman et al. 1988).

Three point sources were identified in the IRAS Point Source Catalog coincident within 10′ radius around the center of DC 314.8–5.1, namely IRAS 14451–6502, IRAS 14437-6503, and IRAS 14433-6506; and no sources were identified in the Faint Source Catalog (Beichman et al. 1988). Source IRAS 14451–6502 is associated with HD 130079, with high-quality detections in the first three bands and moderate-quality detection in the 100 μm band, see Table 1. IRAS 14437-6503 was identified in Bourke et al. (1995a), along with HD 130079, to be associated with DC 314.8–5.1. However, IRAS 14437-6503 corresponds to the Gaia DR3 source 58490393345 15066624 with a Gaia-measured parallax of 0.073 ± 0.0967 corresponding to a distance measured by Bailer-Jones et al. (2021) in the range 4.4–10.4 kpc and as such is not physically related to the cloud. IRAS 14433-6506 is located at the outskirts of the cloud and associated with the Gaia DR3 source 5849037788326819072 with a Gaia-measured parallax of 0.866 ± 0.027 corresponding to a distance measured by Bailer-Jones et al. (2021) of $\simeq$1.1 kpc and as such is determined to not be associated with DC 314.8–5.1.

The right panel of Figure 1 presents the 60 μm IRAS map of DC 314.8–5.1, with an angular resolution of $\sim 1'$ (Beichman 1988). The far-infrared intensity is shifted to the east of center by $\sim 3\farcm5$, likely due to heating by HD 130079.

2.3. ROSAT

A weak X-ray point source is present in the second ROSAT All-Sky Survey (2RXS), with the survey having an effective angular resolution of $1\farcm8$ (Boller et al. 2016), suggesting that DC 314.8–5.1 could be an X-ray emitter. The source position for ROSAT J144833.7–651738 is $1\farcm8$ to the south of the cloud center (see Figure 6 in Appendix B), but still contained within the cloud's boundary per Table 1 denoted as "2RXS." The low photon count of 8 ± 4 counts in the 0.1–2.4 keV band of the ROSAT position-sensitive proportional counters (PSPCs) is insufficient for any meaningful spectral modeling.

2.4. Spitzer

The Spitzer Space Telescope observational data for this work, obtained from the NASA/IPAC Infrared Science Archive (IRSA), were originally acquired with the Infrared Array Camera (IRAC; Fazio et al. 2004) and the Multiband Imaging Photometer (MIPS; Rieke et al. 2004, Proposal ID 50039; P.I.: D. Whittet). DC 314.8–5.1 was observed for a total of 6 hr in 2008 October in five infrared bands: 3.6, 4.5, 5.8, and 8.0 μm with IRAC, and 24 μm with MIPS, with angular resolutions of $\sim 2''$ and $\sim 6''$, respectively.

Due to the presence of many bright sources within the field, we performed artifact correction utilizing the IRAC artifact mitigation tool, by following a procedure similar to that in the Spitzer Data Cookbook,[9] and additional tools listed within, to produce mosaic maps in each band. The resulting 5.8 μm IRAC image is shown in the upper right panel of Figure 2, while all four IRAC images are shown in Appendix A as Figure 5. Reduction of the MIPS data similarly followed recipe 22 in the Spitzer Data Cookbook using MOPEX (Makovoz et al. 2005). The resulting MIPS 24 μm map of the region is shown in the top left panel of Figure 2.

2.5. WISE

WISE was an all-sky survey mission covering the entirety of the Northern and Southern hemispheres. The telescope obtained measurements in four bands (W1–W4) centered at 3.4, 4.6, 12, and 22 μm with resolutions of $6\farcs1$, $6\farcs4$, $6\farcs5$, and $12''$, respectively (Wright et al. 2010).

2.6. Digitized Sky Survey

The spatial extent of DC 314.8–5.1 was delineated by Whittet (2007) based on the spatial distribution of opacity seen in the Digitized Sky Survey (DSS) image, shown here as Figure 2, bottom left panel. We note that the maximum visual extinction of the cloud core, A_v, according to Whittet is $\gtrsim$8.5 mag through the center of the core and decreases toward the outer regions.

[9] https://irsa.ipac.caltech.edu/data/SPITZER/docs/

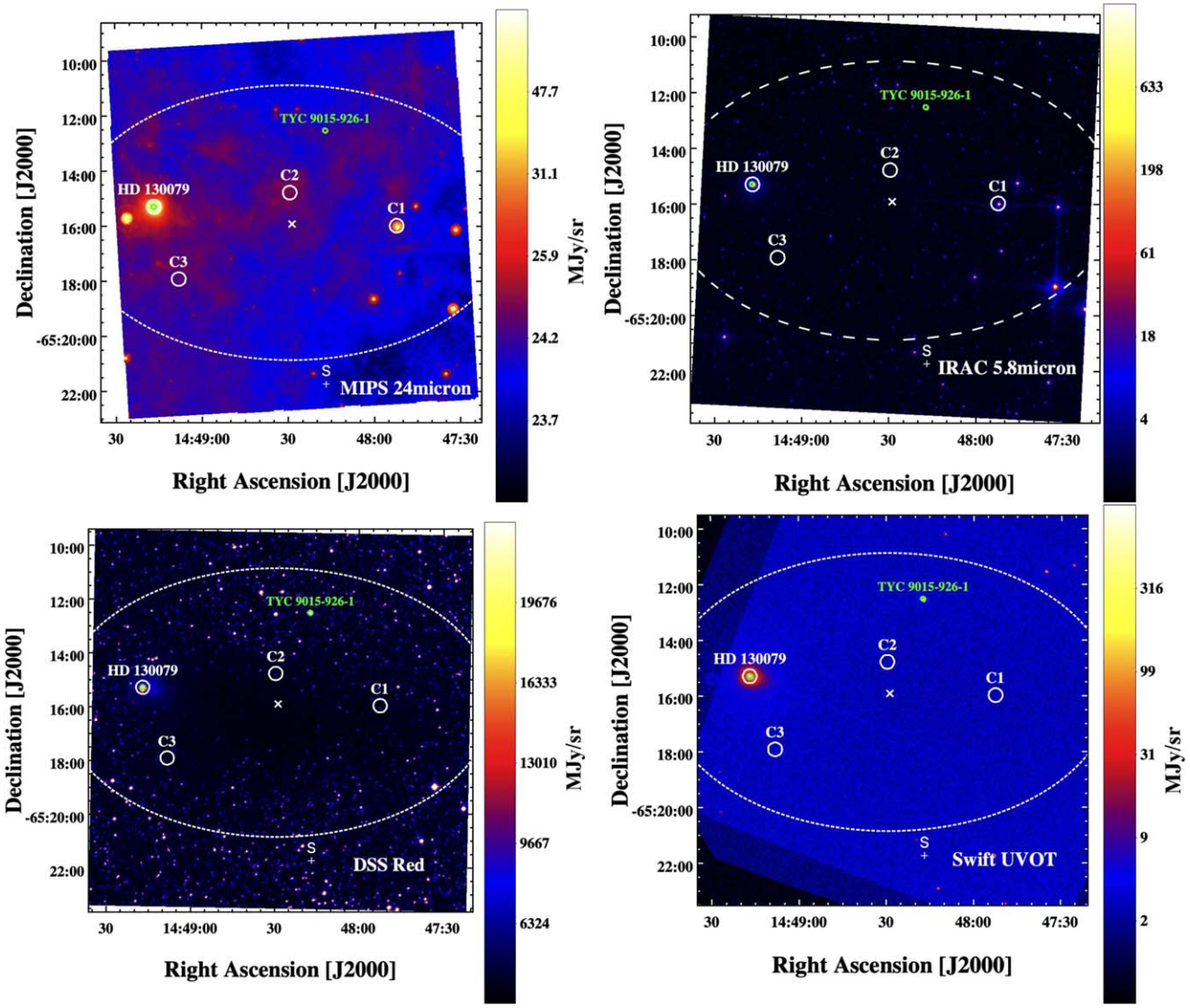

Figure 2. DC 314.8–5.1 region as seen at different wavelengths. Top left: Spitzer MIPS 24 μm log-scaled intensity mosaic map; top right: Spitzer IRAC 5.8 μm log-scaled intensity mosaic map; bottom left: DSS red linear scaled image (700 nm); bottom right: Swift UVOT M2–2250 Å band log-scaled map. In each panel, the white dashed ellipse denotes the globule with the central position marked by a white "×." The green ellipses mark UVOT-detected sources with HD 130079 marked on the left and TYC 9015-926-1 marked near the northern boundary of the globule. "C1" marks the YSO candidate identified by Whittet (2007). "C2" and "C3" mark the potential YSO candidates identified in this work. The X-ray source detected with Swift-XRT is indicated by "S" with a cross.

2.7. *Swift-XRT and UVOT*

Swift Target of Opportunity observations of DC 314.8–5.1 were obtained with the Swift X-Ray Telescope (XRT) instrument (Burrows et al. 2000), as well as the Ultraviolet Optical Telescope (UVOT; Roming et al. 2005) filter of the day, in this instance the UVM2–2250 Å band (Proposal ID: 16282, Requester: E. Kosmaczewski). The target was observed for 3 ks on 2021 September 26. Swift-XRT observations were taken in photon counting mode. Three Swift-XRT images were produced utilizing the Swift-XRT data products generator: the entire spectral range from 0.3 to 10 keV, the soft band from 0.3 to 2.0 keV, and the hard band from 2 to 10 keV. The procedure for image creation followed Evans et al. (2020).

The resulting UVOT M2–2250 Å band image of the DC 314.8–5.1 region is shown in the bottom right panel of Figure 2. The XRT maps of the cloud are shown as Figure 3, including the full-band image from 0.3 to 10 kev (top panel), the soft-band image from 0.3 to 2.0 keV (bottom left), and the hard-band image from 2 to 10 keV (bottom right). Images have been smoothed to aid in visualization (Joye & Mandel 2003), utilizing a Gaussian profile with a radius of 6 px, and $\sigma = 3$ px.

Source detection was performed for each of the three Swift-XRT Point Source Catalogue energy bands (i.e., 0.3–1.0 keV, 1–2 keV, 2–10 keV), as well as for the total energy range (0.3–10 keV), following Evans et al. (2020). No sources were found within the individual narrow bands, and only one low-significance source, denoted hereafter as "S," was detected within the total energy range. The location of the source S (see Table 1) places it at, or just beyond, the periphery of the cloud. The error in the position measurement is $6\farcs9$, and the off-axis angle of the XRT source is $5\farcm8$. The source was detected with $C = 8$ counts including background counts, with average background $B \simeq 0.5$ counts. The corresponding errors, calculated according to Gehrels (1986), as appropriate in the regime

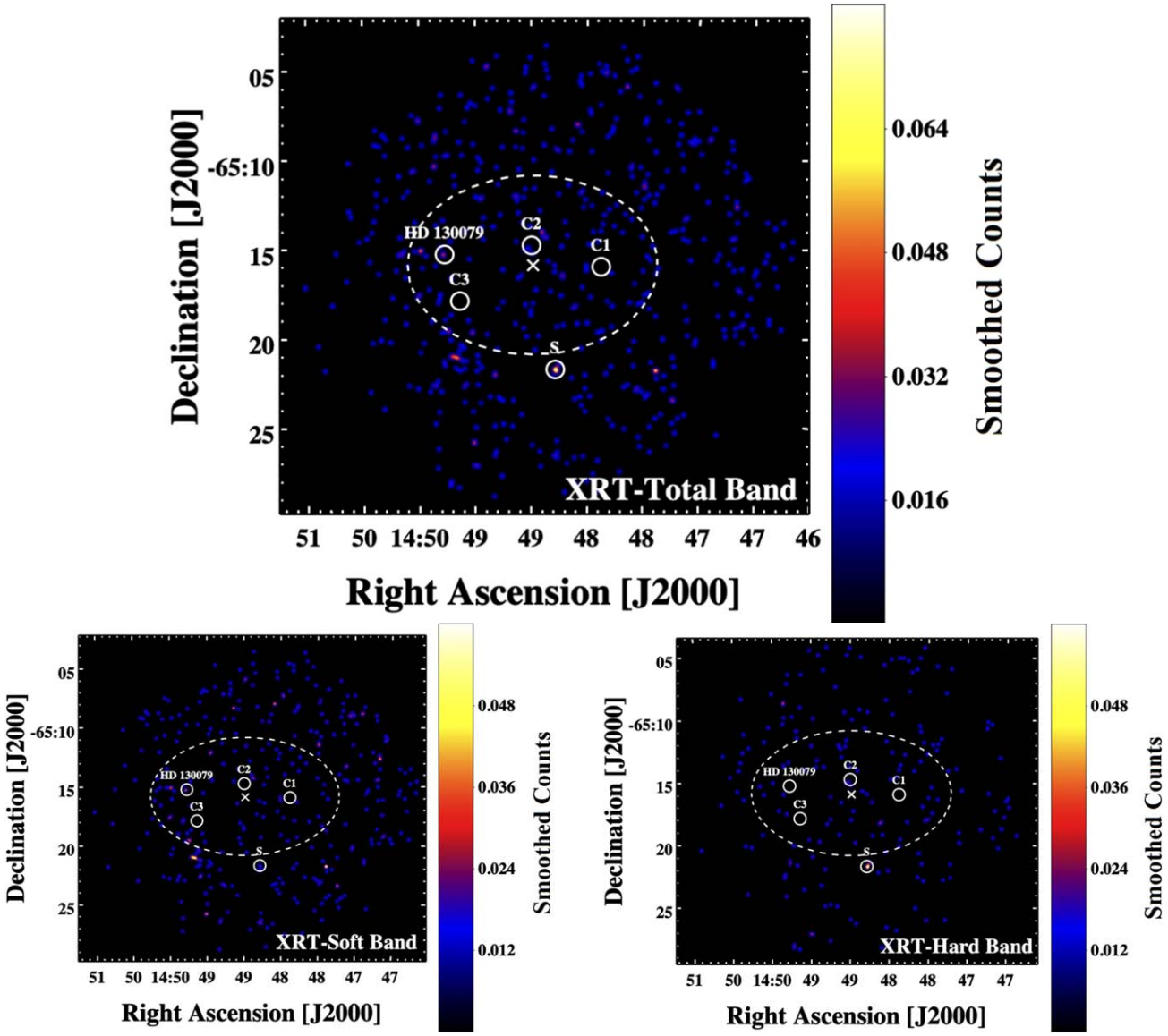

Figure 3. Top: full-band 0.3–10 keV Swift-XRT image of the DC 314.8–5.1 region, smoothed with a Gaussian of radius 6 pixels. The field star HD 130079 is marked in the left of each image. "C1" marks the YSO candidate identified by Whittet (2007). "C2" and "C3" mark the potential YSO candidates identified in this work. The color bar indicates the linear intensity scale for the smoothed (averaged) counts. Bottom left: soft band 0.3–2.0 keV; bottom right: hard band 2–10 keV.

of very low photon statistics (see Evans et al. 2014), are

$$\sigma_C = 1.0 + \sqrt{C + 0.75} \simeq 4.0 \quad (1)$$

and analogously $\sigma_B \simeq 2.1$, leading to a signal-to-noise ratio (S/N) for the detection of

$$\mathrm{S/N} = \frac{C - B}{\sqrt{\sigma_C^2 + \sigma_B^2}} \simeq 1.6. \quad (2)$$

The source "S" can be seen at a low level in the hard-band image but it is not distinguishable in the soft-band image (see bottom panels in Figure 3), which may indicate a hard X-ray spectrum for the source. However, the low photon numbers prevent further characterization of its spectrum. An additional peak can be seen in the lower left just outside the cloud core in the total (top panel) and soft band (bottom left panel) in Figure 3. However, this peak fails to meet $\sigma \geqslant 1$ and as such is not discussed further here.

The Swift UVOT source extraction was performed utilizing the standard "uvotdetect" routine (Roming et al. 2005). We detected a total of 38 sources to a detection threshold of 5σ. Only two sources (see the bottom left panel of Figure 2) are detected within the extent of the cloud, with the brightest being HD 130079. The second source is a star, TYC 9015-926-1, in the northern region of the cloud, see Table 1. It has a Gaia-measured parallax of 2.167 ± 0.015 mas, corresponding to a Bailer-Jones et al. (2021) distance range of $453.4 - 459.7$ pc. Therefore, this object is a (somewhat) nearby star located behind the cloud.

3. Identification of YSOs

The evolutionary progression of the infrared emission of YSOs is such that the wavelength of the blackbody peak emission migrates toward the near-infrared as the YSO ages, while the far-infrared excess (due to the surrounding dusty disks and/or envelopes) decreases (see, e.g., Greene et al. 1994;

André et al. 2014). This results in the population of the youngest YSOs, i.e., Class 0 sources, emitting almost exclusively in the submillimeter/far-infrared range. On the other hand, Class I–III sources, which emit efficiently at shorter wavelengths, should, if present, manifest in the analyzed mid-infrared surveys (see in this context Evans et al. 2009; Gutermuth et al. 2009). Class I sources are deeply embedded protostars with infalling, dense envelopes, characterized by a rising or flat mid-infrared spectrum. Class II sources denote YSOs that are pre-main-sequence stars with gas-rich optically thick disks and ongoing accretion onto the central star, and a decreasing mid-infrared spectrum. Finally, Class III YSOs have gas-poor disks and very little infrared excess due to dust, and are notoriously difficult to separate from young main-sequence stars. We also discuss here the so-called "transition disk" objects, which are YSOs without an inner disk but containing an optically thick outer disk (André et al. 2014).

3.1. Class 0 Source Limits

The Point Source Catalog for IRAS identified no candidate sources within our system down to luminosity levels 6.7×10^{32} erg s^{-1} ($\sim$0.18 $L_{\odot}$) for 60 and 100 μm, see Section 2.2. This luminosity level indicated that our study is sensitive to YSO Class 0 sources down to core masses $\sim$0.1 $M_{\odot}$ (Dunham & Vorobyov 2012). The lack of any source detections associated with the cloud, with the exception of HD 130079, strongly suggests the absence of YSO Class 0 sources within the system.

3.2. Spitzer IRAC and 2MASS Source Examinations

The Spitzer IRAC mapping data, for the observed frame time of 12 seconds, effectively probe down to flux levels of 52 μJy at 8 μm and 6.1 μJy at 3.6 μm with a spatial resolution of $\sim 2''$ (Fazio et al. 2004). At the distance of the cloud (432 pc), these limits correspond to monochromatic luminosities of $\simeq 4.4 \times 10^{29}$ erg s^{-1} and $\simeq 1.2 \times 10^{29}$ erg s^{-1}, respectively. The observed 3.6 μm range (3.1–3.9 μm), in particular, is rather close to the peak of the blackbody emission component in Class I–III sources, and as such the latter value should serve as a good proxy for the limiting luminosity of YSO candidates, with the bolometric correction of the order of a few at most (see, e.g., Lada 1987). In other words, in the Spitzer IRAC mapping data, we are sensitive to YSO Class I–III luminosities as low as $\sim 10^{-4}$ $L_{\odot}$, so that any young star with a core mass down to 0.01 $M_{\odot}$ (see Dunham & Vorobyov 2012), should easily be detected.

We performed a search with a radius of 5′ around the central position of the cloud, see Table 1, with the Spitzer Enhanced Imaging Products (SEIP) source list in order to identify potential YSOs. We restricted our sample to a signal-to-noise $S/N > 5$ in all four IRAC bands, excluding unresolved extended sources and excluding sources with only upper limits in any band (sources detected in only some bands are considered in the follow-up selection). This returned a total of 1319 sources within the sampled region.

First, we applied the color criteria from Gutermuth et al. (2009), Appendix A.1 therein, to the sample of 1319 sources. This removed 132 star-forming galaxies (SFGs) and 256 active galactic nuclei (AGNs), resulting in a sample of 924 potential YSOs. *None* of these sources met the criteria to be identified as a Class I or Class II YSO as defined in Gutermuth et al. (2009).

Second, we investigated sources with lower significant detections, following the cuts presented in Winston et al. (2019), Appendix A.2 (Equations (17)–(20)). Specifically, we investigated those sources that are lacking robust ($S/N < 5$) detections in IRAC 5.8 μm or IRAC 8.0 μm, but still show $S/N > 5$ detections in IRAC 3.6 μm and IRAC 4.5 μm, with the requirement that they also have significant ($\sigma < 0.1$ mag) detections in 2MASS bands H and K_s. However, we find no sources within this sample that meet the color criteria needed for a YSO detection as defined in Winston et al. (2019).

Further, we searched for deeply embedded protostars, in the so-called "Phase 3" cuts adopted by Gutermuth et al. (2009), Appendix A.3 therein. We included sources from SEIP that lack detections in IRAC 5.8 μm or IRAC 8.0 μm bands, are bright in the MIPS 24 μm band, and have strong ($S/N > 5$) detections in IRAC 3.6 μm and IRAC 4.5 μm. Our selection returned 164 sources, including some previously flagged as AGNs based on the IRAC color cuts. However, only three sources met the MIPS 24 μm band brightness criteria of $[24] < 7$ mag. None of these three sources satisfied the remaining criteria to be identified as a YSO, and as such this selection returned no candidate sources.

Finally, we comment here on the remaining sources not classified in the first Gutermuth et al. (2009) cuts adopted here; see the right panel in Figure 7 of Appendix C. Sources that fall in this range are often consistent with Class III sources (see Dunham et al. 2015; Anderson et al. 2022, for further discussion). However, these regions of infrared colors are heavily contaminated by asymptotic giant branch (AGB)-type background stars. Dunham et al. (2015) estimated that contamination in the Class III type sources by background stars ranges from 25% to 90% in their sample. In order to disentangle background stars from true Class III sources, we further inspected these remaining 923 sources with Gaia, below.

3.3. Gaia Parallax Measurements

We inspected the remaining 923 IRAC sources unidentified by the Gutermuth et al. (2009) cuts, which are likely background stars or Class III candidates (see Section 3.2), with the Gaia source catalog (Gaia Collaboration et al. 2021). Gaia parallaxes provide precise measurements with a spatial resolution of 0.″4 and so are capable of separating individual objects even when clustered on the sky.

The source "C1," not identified above as a bona fide YSO, but previously identified as a potential candidate by Whittet (2007), has a Gaia-measured parallax of 0.073 ± 0.096 mas. The Bailer-Jones et al. (2021) catalog marks the distance to this star as $6.67^{+3.75}_{-2.25}$ kpc, which is far beyond DC 314.8–5.1.

We looked at a sample of Gaia sources within the same region inspected by IRAC, out to a radius of 5′ around the central position of the cloud, see Table 1. We additionally constrained the list of Gaia sources to those having a parallax measurement (within the error bounds) coinciding with the parallax for HD 130079, i.e., 2.2981 ± 0.0194 mas. To cross-check with the 923 IRAC sources, we investigated each IRAC source for any "good" Gaia source within the IRAC spatial resolution of $\sim 2''$ (Fazio et al. 2004). This resulted in a sample of 27 potential Class III/field star sources. We further cross-checked this sample with the Bailer-Jones et al. (2021) catalog for measured distances consistent with HD 130079 ($\sim$427–435 pc). We identified two sources, SSTSL2 J144829.

39-651448.5 and SSTSL2 J144907.95-651756.4, corresponding to the Gaia DR3 sources, numbers 3584903675753468953 6 and 5849041288680373504, with appropriate distance measurements, denoted hereafter as "C2" and "C3," as in Table 1.

3.4. Pre-main-sequence Stars in Swift-XRT Data

PMSs are established X-ray emitters, with corresponding X-ray luminosities 10–10,000 times above the levels characterizing the old Galactic disk population (e.g., Preibisch & Feigelson 2005; Montmerle et al. 2000). They are routinely detected with the Chandra X-ray Observatory in molecular clouds because their keV photons penetrate heavy extinction (e.g., Wang et al. 2009; Kuhn et al. 2010). The bright members of PMS populations revealed by such studies are typically well modeled assuming a plasma in collisional ionization equilibrium, using the Astrophysical Plasma Emission Code (APEC; Smith et al. 2001), with temperatures of the order of a few to several keV, low metal abundances, and 0.5–10 keV luminosities of the order of 10^{30} erg s^{-1}.

Here, we compare the expected X-ray levels of PMSs in DC 314.8–5.1 with X-ray luminosity of the source "S" detected in the Swift-XRT pointing. We calculate the Galactic hydrogen column density in the direction of DC 314.8–5.1, utilizing the NHtot tool provided through HESEARC (HI4PI Collaboration et al. 2016). Given that the source is only at a distance of 432 pc, the resulting values of $N_{\rm H,Gal} \simeq 3.2 \times 10^{21}$ cm^{-2} is likely an overestimation for the real column density along the line of sight. Nonetheless, in all the flux estimates below we conservatively adopt the value $N_{\rm H,Gal} \simeq 3 \times 10^{21}$ cm^{-2} .

In addition to the Galactic diffuse interstellar medium (ISM) fraction, we take into account the intrinsic absorption within the cloud. For this, assuming the cloud's mean gas density of 10^4 cm^{-3} and a spatial scale of 0.3 pc, the corresponding column density is estimated at the level of $N_{\rm H,int} \simeq 10^{22}$ cm^{-2}. Again, this should be considered as an upper limit for the intrinsic absorption value.

For the APEC spectral model with temperature $kT = 2$ keV, metallicity $Z = 0.2\,Z_\odot$, and the absorbing column densities as estimated above, the 0.3–10 keV XRT observed count rate integrated over all solid angle, $4.1^{+1.8}_{-1.4} \times 10^{-3}$ counts s^{-1}, corresponds to an unabsorbed flux of $F_{0.3-10\,\rm keV} \simeq 4^{+1.7}_{-1.4} \times 10^{-13}$ erg cm^{-2} s^{-1}. The isotropic intrinsic luminosity of $L_{0.3-10\,\rm keV} \simeq 0.9^{+0.4}_{-0.3} \times 10^{31}$ erg s^{-1} would be $2 \times 10^{-3}\,L_\odot$ if at the distance of DC 314.8–5.1. However, by decreasing the intrinsic column density down to $N_{\rm H,int} \simeq 10^{21}$ cm^{-2}, as would be a more appropriate estimate at the far outskirts of DC 314.8–5.1, the implied intrinsic luminosity decreases to $L_{0.3-10\,\rm keV} \simeq 4.9^{+2.1}_{-1.7} \times 10^{30}$ erg s^{-1} $\sim 10^{-3}\,L_\odot$.

For comparison, main-sequence high-mass stars are established sources of soft X-ray emission, characterized by an approximately linear luminosity scaling with bolometric photospheric emission, $\log(L_{\rm X}/L_{\rm bol}) \simeq -7$ (Güdel & Nazé 2009). Yet PMSs are relatively brighter in X-rays, especially in the low-mass range. Indeed, the recent analysis by Getman et al. (2022) showed that, for PMS systems with masses of $0.1 - 2\,M_\odot$, the ratio $\log(L_{\rm X}/L_{\rm bol})$ can be found in a broad range from $\lesssim -4$ up to $\gtrsim -2$, with the median just below the saturation level[10] of –3. This ratio, however, falls rapidly above $2\,M_\odot$.

[10] In cool young stars characterized by rapid rotation, the coronal X-ray luminosities powered by magnetic activity are observed to saturate at the $\log(L_X/L_{\rm bol}) = -3$ level (Vilhu & Walter 1987; Stauffer et al. 1994).

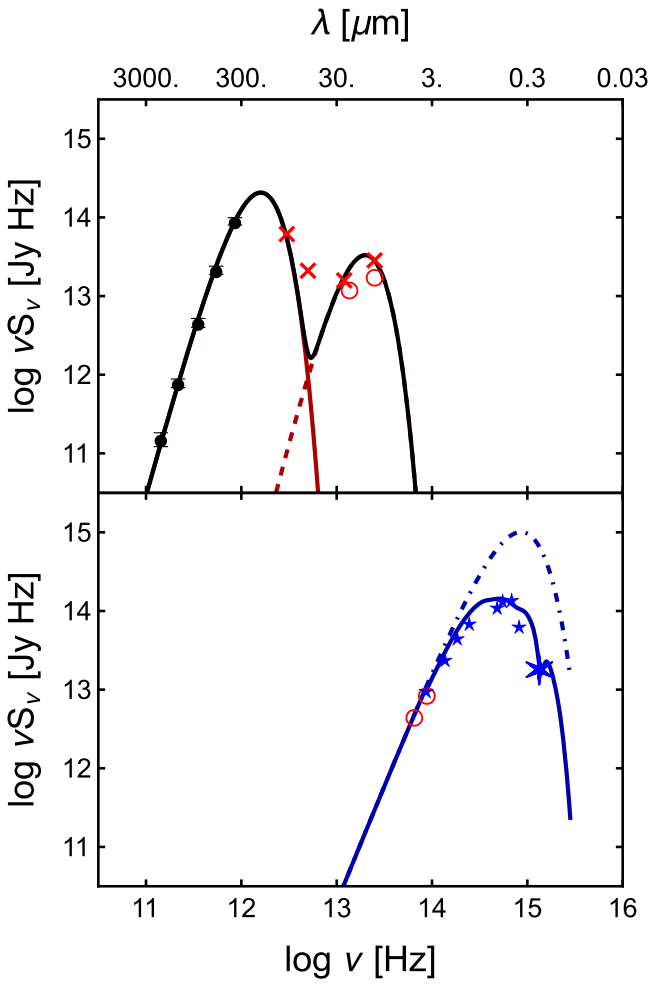

Figure 4. Top: SED of the DC 314.8–5.1 system, based on observations with Planck (filled black circles), IRAS (red crosses), and WISE (open red circles). Dark red solid and dashed curves represent modified blackbody models for the emission of cold (14 K) and warm (160 K) gas within or on the surface of the cloud, respectively; the black solid curve denotes the superposition of the two. Bottom: SED of HD 130079 from ground-based telescopes and the Gaia survey (small blue stars), WISE (open red circles), and finally with the Swift UVOT (big blue star). The dark blue dotted–dashed curve corresponds to the intrinsic emission of the field star HD 130079, modeled as a blackbody with the temperature 10,500 K and a total luminosity of 3×10^{35} erg s^{-1}; the dark blue solid curve illustrates this intrinsic emission subjected to the interstellar reddening. See Section 4 for a description.

During the first few million years, the X-ray luminosity of PMSs appears to be approximately constant, declining with time at later evolutionary stages, and again more rapidly as stellar mass increases (Getman et al. 2022). Only a small fraction of the $<2\,M_\odot$ systems appears brighter than 3×10^{30} erg s^{-1} in X-rays, and those cases are believed to represent super- and mega-flaring states (e.g., Getman & Feigelson 2021). More than 75% of the more massive $(2 - 100\,M_\odot)$ systems, on the other hand, exceed 3×10^{30} erg s^{-1}. As such, at the Swift-XRT luminosity level of $L_{0.3-10\,\rm keV} \simeq 4.9^{+2.1}_{-1.7} \times 10^{30}$ erg s^{-1}, we are unlikely to detect single PMSs, other than the brightest super/mega-flaring sources.

The search for possible infrared counterparts for the Swift-XRT source "S" returns two WISE/2MASS sources, with $\sim 8''$–$9''$ separations from the position of source "S." The WISE colors for J144815.66-652141.9 (W1 – W2 = –0.62 and W2 – W3 $\geqslant$ 4.18) indicate that the object could be a background luminous infrared galaxy (LIRG) or a starburst galaxy. The

WISE colors of J144818.35-652144.7 (W1 − W2 = −0.31 and W2 − W3 ⩾ 2.37), on the other hand, are consistent with a regular star-forming galaxy (see Wright et al. 2010). One of these two sources is a likely counterpart of the Swift-XRT source "S," although neither of them represents a viable PMS candidate.

Furthermore, ROSAT J144833.7–651738, detected with a 448.83 s exposure by ROSAT and discussed above in Section 2.3, is not observed with the 3 ks observation by Swift-XRT, see Figure 3. A comparison of the ROSAT and Swift-XRT maps is shown in Figure 6 of Appendix B. This lack of a detection may indicate that ROSAT J144833.7–651738 is an artifact of the 2RXS analysis, or potentially a transient/variable source.

4. Discussion

YSOs can be separated from background stars due to the presence of infrared excesses, primarily in the 1–30 μm range (Evans et al. 2009). As such, if present and related to the cloud, YSOs may appear as optical/infrared point sources, for which parallax distances should be similar to the distance of DC 314.8–5.1. In this context, we investigated the point sources located within the spatial extent of DC 314.8–5.1 that survived the selection cuts applied following Winston et al. (2019) and Gutermuth et al. (2009) and with appropriate Gaia parallax and Bailer-Jones et al. (2021) distances. Two sources were identified in this way as potential Class III candidates: "C2" and "C3."

Dunham et al. (2015) proposed the [3.6] − [24] ⩽ 1.5 color values for separating likely Class III sources from AGB field stars. Utilizing this cut, and the 3σ upper limit for the 24 μm fluxes, we found color values of −0.66 and 2.35 for C2 and C3, respectively. We can, however, rule out the likelihood of "C3" being a Class III YSO based on its location near the outer edge of the core region. This is because, on the outskirts of the cloud, we expect a lower level of extinction ∼2–3 (see Whittet 2007; Kosmaczewski et al. 2022), and so for a Class III source in the evolutionary stage, we would expect to see some evidence of an optical/near-IR reflection nebula (van den Bergh & Herbst 1975; Connelley et al. 2007). The lack of a detectable reflection nebula for "C2," on the other hand, is unsurprising because "C2" is located near the central region of the core with extinction levels >8.5 mag (Whittet 2007). Yet this region is also the coldest region (see left panel of Figure 1) with a Planck-measured temperature of ∼15 K. A Class III source would be expected to produce significant heating of the dust surrounding it, and that is not seen in DC 314.8–5.1 using available observations (Strom et al. 1975). For these reasons, we consider the identification of "C2" as a Class III YSO to be unlikely. However, detailed spectral modeling combined with deeper X-ray measurements would be necessary to substantiate this claim (see Dunham et al. 2015).

The lack of any robust YSO detections further supports the prestellar state of DC 314.8–5.1, as discussed in Whittet (2007) and Kosmaczewski et al. (2022). However, younger YSOs (Class 0) and sources that are still heavily embedded within their cores may not be detectable by mid-infrared excesses (Evans et al. 2009; Karska et al. 2018). In order to exclude the presence of such objects deep far-infrared, CO, and/or X-ray observations are needed (Grosso et al. 2000).

The short Swift-XRT exposure we have obtained is sensitive to sources within the cloud down to an unabsorbed 0.5–10 keV luminosity level of $\lesssim 10^{31}$ erg s^{-1}. Given this level, only the brightest PMSs could be detected and, among the low-mass (<2 $M_{\odot}$) systems, only young flaring objects would be seen. A much deeper X-ray imaging observation would be needed to constrain the potential PMS population in DC 314.8–5.1 (Kuhn et al. 2010; Getman et al. 2022).

The spectral energy distribution (SED) of DC 314.8–5.1, within the spectral range from microwaves up to UV, has three main components: the thermal emission of the dominant cold dust, the emission of a warm dust photoionized and heated by the field star, HD 130079, and the photospheric emission of HD 130079 itself. These are presented in Figure 4.

We consider the cloud components and the HD 130079 starlight separately (top and bottom panels of Figure 4, respectively). For the microwave segment of the cloud SED, dominated by cold dust, we take aperture fluxes from the Second Planck Catalogue of Compact Sources (PCCS2E; Planck Collaboration et al. 2016b) at 143, 217, 353, 545, and 857 GHz. In the infrared range, dominated by the radiative output of the warm dust in the cloud's regions adjacent to the star, we use fluxes from the IRAS Point Source Catalog v.2.1 at 12, 25, 60, and 100 μm, and the WISE fluxes at 3.4, 4.6, 12, and 22 μm, all corresponding to the infrared source IRAS 14451–6502 associated with HD 130079 (see Section 2.2). Indeed as seen in Figure 1, the IRAS and (to a lesser extent) the Planck images display a maximum peak shifted away from the center of DC 314.8–5.1. The different apertures and resolutions of the Planck (5′), IRAS (1′), and WISE (6″–12″) instruments could be important though. These differences are particularly relevant in the case of the IRAS versus WISE comparison and could explain the lower WISE fluxes when compared to the IRAS photometry within the overlapping wavelength range of 12–25 μm.

We have calculated several model curves for the cold thermal component using a modified blackbody emission $B_{\nu}(T) \times (\nu/\nu_0)^{\beta}$. Our findings indicate that the best-matching model corresponds to a temperature of $T = 14$ K, consistent with the PGCC model fit, and a spectral index of $\beta = 1.5$ (see the dark red solid curve in Figure 4; see Section 2.1). The far/mid-infrared (roughly 7–70 μm) emission of the system is a complex superposition of the continua from multitemperature dust, molecular lines, and PAH features, all generally decreasing in intensity with distance away from the photo-ionizing star DC 314.8–5.1 (see Kosmaczewski et al. 2022). As a basic representation of the entire spectral component, we adopt the simplest model, which consists of a single modified blackbody. This time, the model has a temperature of 160 K, a spectral index of $\beta = 2.0$, and a normalization adjusted to match the 12–25 μm IRAS fluxes (see the dark red dashed curve in Figure 4).

While the temperature of the cold component is precisely constrained by the multiwavelength (143–857 GHz) Planck data in conjunction with the IRAS 100 μm photometry, the warm component's temperature lacks such precision. As previously emphasized, using a single modified blackbody to approximate the hot dust emission in the system is a basic, zero-order approximation. It is worth noting that the IRAS 60 μm flux, which surpasses both the cold (14 K) and warm (160 K) blackbody emission components, indicates the

presence of gas with intermediate temperatures in the system. As such, this model is meant to be primarily illustrative.

For the SED representing the HD 130079 starlight, the near-infrared (filters *JHKL*) and optical (*UBV*) fluxes follow directly from the compilation by Whittet (2007, see Table 1 therein), with the addition of the *G*-band flux from the EDR3 (Gaia Collaboration et al. 2021), and the UV 2250 Å flux measured from the newly obtained Swift UVOT observations (see Section 2.7). The photospheric emission of HD 130079 is modeled here assuming a simple optically thick blackbody spectrum with the temperature $T_\star = 10{,}500$ K, such that the bolometric stellar luminosity is $L_\star = 4\pi R_\star^2\, \sigma_{\rm SB} T_\star^4 \simeq 3 \times 10^{35}$ erg s^{-1}, for the stellar radius $R_\star = 2.7 \times R_\odot$ and the distance of 432 pc. This intrinsic emission (denoted in Figure 4 by the dark blue dotted–dashed curve) is next reduced by interstellar reddening using the Cardelli et al. (1989) empirical extinction law with the coefficients as given in Equations (2)–(5) of Cardelli et al., and values for E_{B-V} (= 0.395) and R_V (= 4.5, in excess over the averaged ISM value of 3.1) adopted from Whittet (2007). The reddened starlight (given by the solid dark blue curve in Figure 4) matches the near-infrared–to–UV fluxes of the star including the 3.4 and 4.6 μm WISE fluxes and the Swift UVOT 2250 Å flux, even though no stellar photospheric reddening was included in this simple model.

The mass of the Planck source PGCC G314.77–5.14 has been estimated in Planck Collaboration et al. (2016a) as

$$M = \frac{D^2 F_\nu}{\kappa_\nu B_\nu(T)} \simeq 10 \pm 14\, M_\odot, \tag{3}$$

based on the measured 857 GHz flux density F_ν integrated over the solid angle $\Omega = \pi\theta^2/4$ (where θ is the geometric mean of the major and minor FWHMs), which is effectively half the provided PGCC flux, with the dust opacity value $\kappa_\nu = 0.1(\nu/1\,{\rm THz})^2$ cm^2 g^{-1} adopted from Beckwith et al. (1990). Meanwhile, Whittet (2007) estimated the mass of the *core* of the globule to be $\gtrsim 50\, M_\odot$ when updated for the distance of 432 pc. However, this discrepancy might not be significant, keeping in mind that the Planck estimate provides upper 2σ (95%) and 3σ (99%) confidence limits of 68 $M_\odot$ and 115 $M_\odot$, respectively. These limits arise solely from uncertainties in flux and distance estimates and do not account for the uncertainty in the dust opacity function, κ_ν (see in this context the discussion in Beckwith et al. 1990, specifically Section IIIe, and also D'Alessio et al. 2001).

The mass of the cloud—as an isolated dark cloud at high Galactic latitudes—can also be estimated from the excess absorption seen in X-rays toward the cloud (see in this context Sofue & Kataoka 2016) and from the high-energy γ-ray data as measured by Fermi's Large Area Telescope (LAT; see Mizuno et al. 2022, and references therein). In the former case, a much deeper X-ray observation would be needed to estimate the absorbing hydrogen column density across the cloud. Concerning the latter, we note that in the Fermi High-Latitude Extended Sources Catalog by Ackermann et al. (2018), the integrated 1 GeV–1 TeV fluxes of resolved high-confidence sources in the LAT data extend down to a few/several $\times 10^{-10}$ cm^{-2} s^{-1}. Further, those that appear pointlike lie about one magnitude lower, with a median of 2.5×10^{-10} cm^{-2} s^{-1}. An estimate for the flux expected from DC 314.8–5.1 due to the interactions with high-energy CRs (assuming no CR overdensity with respect to the CR background) is

$$F(>E_\gamma) \simeq 2 \times 10^{-13}\, \frac{M/10^5\, M_\odot}{(D/{\rm kpc})^2} \left(\frac{E_\gamma}{1\,{\rm TeV}}\right)^{-1.7} \sim 2 \times 10^{-10}\,{\rm cm^{-2}\,s^{-1}} \tag{4}$$

(see Gabici 2013). In the above, we use $M = 160\, M_\odot$, corresponding to the *total* mass of the cloud (Whittet 2007, updated distance $D = 432$ pc), and $E_\gamma = 1$ GeV. This level of emission may be detected in dedicated Fermi-LAT studies, leading to a robust estimate of the mass in this prestellar, condensed dark cloud.

5. Conclusions

In this paper, we have discussed the multiwavelength properties of the dark globule, DC 314.8–5.1, through dedicated observations with the Spitzer Space Telescope and the Swift-XRT and UVOT instruments, supplemented by the archival Planck, IRAS, WISE, 2MASS, and Gaia data. This investigation of the characteristics of the system, over a wide range of the electromagnetic spectrum, has led to the following conclusions.

1. We have further supported the idea that DC 314.8–5.1 is a prestellar core, with no conclusive Class I–III YSO candidates present within the extent of the system down to luminosities as low as $\sim 10^{-4}\, L_\odot$, translating to a stellar core mass down to 0.01 $M_\odot$ (see Dunham & Vorobyov 2012). We do, however, maintain one possible candidate Class III YSO object ("C2," see Table 1), albeit unlikely due to the lack of heating seen in that region of DC 314.8–5.1. Furthermore, we exclude any younger Class 0 YSO candidates down to luminosities of $\sim 0.18\, L_\odot$, translating to a core mass of $\sim 0.1\, M_\odot$ (see in this context Barsony 1997).
2. With the Swift-XRT observations, we probed for any potential PMS population down to a luminosity level of $\lesssim 10^{31}$ erg s^{-1}. This level would have detected a typical PMS of mass $\geqslant 2$ $M_\odot$, while being capable of only detecting the brightest (flaring) low-mass (<2 $M_\odot$) PMSs. Deeper observations would be needed to reject the presence of lower-mass objects. Furthermore, CO observations of this system could also test for the presence of the youngest, Class 0, protostars (Kirk et al. 2005, and references therein).
3. We investigated the SED of the DC 314.8–5.1 system as well as the nearby illuminator HD 130079. Our analysis confirmed the presence of warm dust, with temperatures $\gtrsim 100$ K, in addition to the dominant 14 K dust component. This warm component manifests itself in the IRAS photometry, particularly within the 12–25 μm range.
4. We comment on the variation in mass estimates of DC 314.8–5.1, ranging from $\simeq 12\, M_\odot$, based on the Planck photometry, up to $\gtrsim 50\, M_\odot$, following from the visual extinction characteristics, for the core of the globule. We point out that the discrepancy may be due to errors in the flux measurement, variations in the methodology, and the uncertainties of the opacity model for this particular system. We also note in this context that the cloud should be detectable in high-energy γ-rays

with Fermi-LAT, given the estimate for the total mass of the globule of $\sim 160\,M_{\odot}$.

Hence, DC 314.8–5.1 remains a prestellar cloud core. This makes it an ideal candidate for deeper observations, particularly in high-energy X-rays and γ-rays.

Acknowledgments

E.K. and Ł.S. were supported by Polish NSC grant 2016/22/E/ST9/00061. This research was completed while E.K. held an NRC Research Associateship award at the Naval Research Laboratory. W.R.M.R. thanks the Leiden Observatory for financial support. A.K. acknowledges support from the First TEAM grant of the Foundation for Polish Science No. POIR.04.04.00-00-5D21/18-00 and the Polish National Agency for Academic Exchange grant No. BPN/BEK/2021/1/00319/DEC/1. C.C.C. was supported by NASA DPR S-15633-Y. W.R.M.R. thanks the European Research Council (ERC) for financial support under the European Union's Horizon 2020 research and innovation program (grant agreement No. 101019751 MOLDISK). The authors thank the anonymous referee for the comments and suggestions, which helped to improve the manuscript.

This work is based on observations made with the Spitzer Space Telescope, obtained from the NASA/IPAC Infrared Science Archive, both of which are operated by the Jet Propulsion Laboratory, California Institute of Technology under a contract with the National Aeronautics and Space Administration.

This work has made use of data from the European Space Agency (ESA) mission Gaia (https://www.cosmos.esa.int/gaia), processed by the Gaia Data Processing and Analysis Consortium (DPAC, https://www.cosmos.esa.int/web/gaia/dpac/consortium). Funding for the DPAC has been provided by national institutions, in particular, the institutions participating in the Gaia Multilateral Agreement. We are grateful to Timo Prusti for advice on Gaia data.

This research used data products from the Two Micron All Sky Survey, a joint project of the University of Massachusetts and the Infrared Processing and Analysis Center, funded by the National Aeronautics and Space Administration and the National Science Foundation. The Digitized Sky Survey was produced at the Space Telescope Science Institute under U.S. Government grant NAG W-2166. The images of these surveys are based on photographic data obtained using the Oschin Schmidt Telescope on Palomar Mountain and the UK Schmidt Telescope. The plates were processed into the present compressed digital form with the permission of these institutions.

Appendix A
Mid-infrared Images of DC 314.8–5.1

In Figure 5, we present the dedicated Spitzer IRAC images of the DC 314.8–5.1 region at 3.6, 4.5, 5.8, and 8.0 μm with a spatial resolution of $\sim 2''$ (Fazio et al. 2004). As is visible in the figure, the superior spatial resolution of the Spitzer instrument allows for the detection of individual point sources within DC 314.8–5.1. Additionally, the diffuse emission of the cloud and some faint irregular structure can be seen in the bottom right panel of Figure 5.

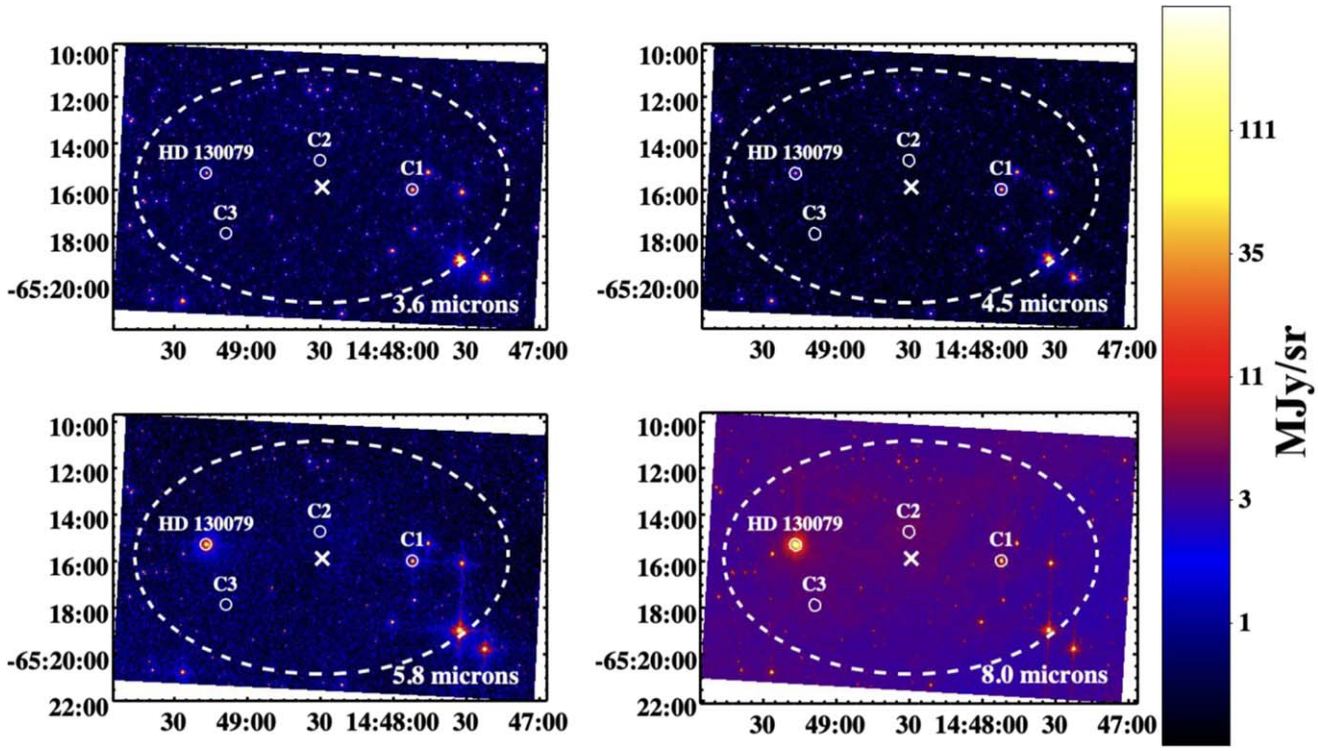

Figure 5. Spitzer IRAC-band maps of the DC 314.8–5.1 region. Top left: channel 1 at 3.6 μm; top right: channel 2 at 4.5 μm; bottom left: channel 3 at 5.8 μm; bottom right: channel 4 at 8.0 μm. The white dashed ellipse marks the optical extent of DC 314.8–5.1. The color bar is set with a minimum of zero and a maximum value of 200 MJy sr^{-1} on a log scale. The field star HD 130079 is marked in the left of each image, "C1" marks the YSO candidate identified by Whittet (2007), and "C2" marks the YSO candidate identified in this work.

Appendix B
ROSAT and Swift-XRT Comparison

In Figure 6, we compare the ROSAT full-band 0.1–2.4 keV image of the DC 314.8–5.1 region with the corresponding images from the Swift-XRT soft band 0.3–2.0 keV as well as the hard band 2–10 keV, including for reference the MIPS 24 μm image of the region. We note that, assuming the emission model specified in Section 3.4, the PSPC 0.1–2.4 keV count rate for ROSAT J144833.7–651738 of 0.0175 ± 0.0082 counts s^{-1} would correspond to the Swift-XRT PC 0.3–10 keV count rate of $(19.7 \pm 9.2) \times 10^{-3}$ counts s^{-1} for $N_{\rm H,int} \simeq 10^{22}$ cm^{-2}, and $(13.1 \pm 6.2) \times 10^{-3}$ counts s^{-1} for $N_{\rm H,int} \simeq 10^{21}$ cm^{-2}, while the estimated XRT 0.3–2.0 keV count rate for the source "S" is $4.1^{+1.8}_{-1.4} \times 10^{-3}$ counts s^{-1}, and the 3σ upper limit at the nominal position of the center of the cloud/ROSAT source, calculated with The Living Swift-XRT Point Source Catalogue online tool,[11] is $\simeq 3 \times 10^{-3}$ counts s^{-1}. The Swift-XRT images have been smoothed for visualization purposes to more closely resemble the resolution of the ROSAT observation using a boxcar with a width of $2r + 1$ pixels and a radius (r) of 3 pixels (Joye & Mandel 2003).

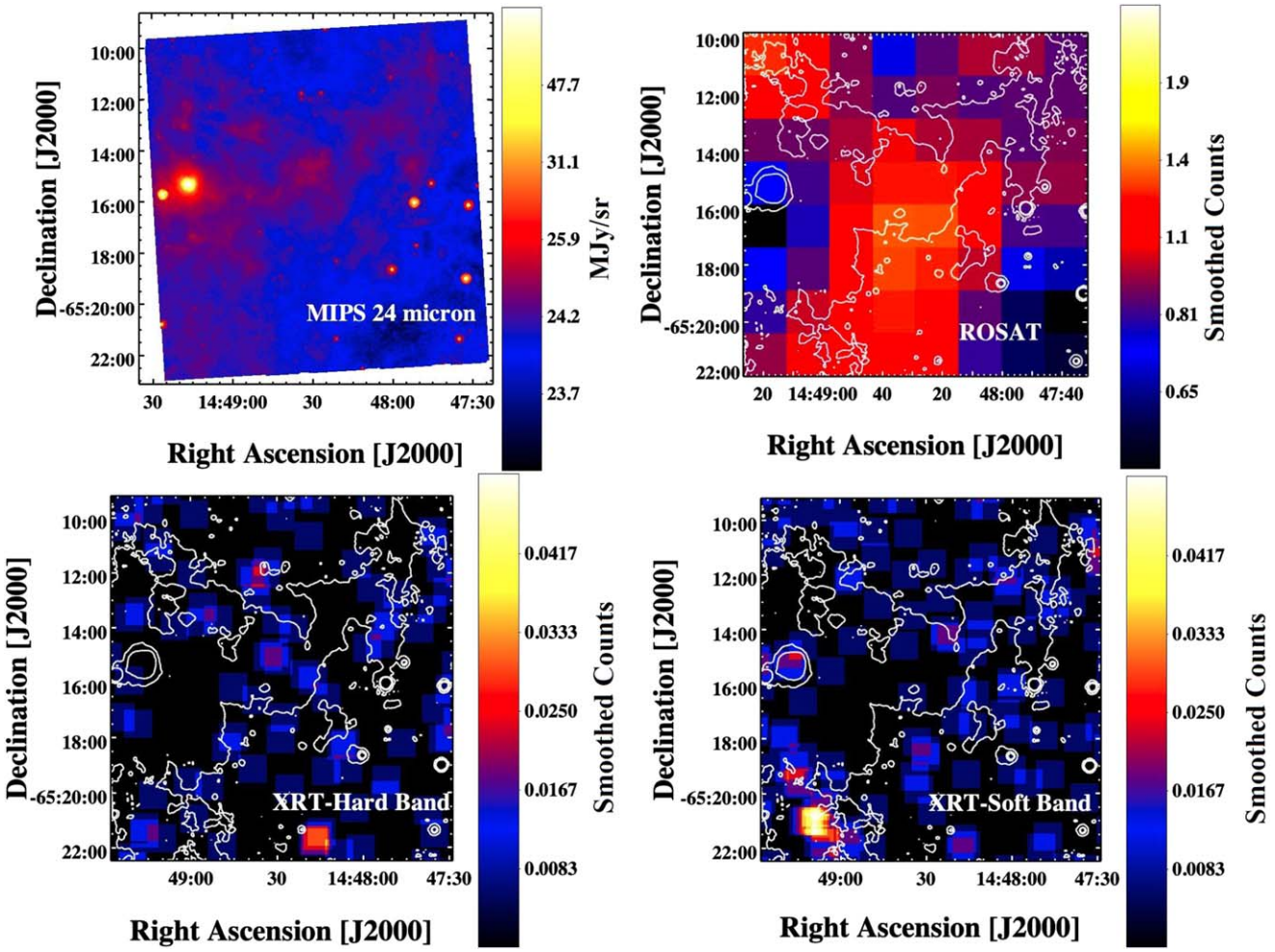

Figure 6. Top left: Spitzer MIPS 24 μm image of the DC 314.8–5.1 region. The color bar spans from a minimum of 23.5 to 100 MJy sr^{-1} on a log scale. White contours in the following panels represent MIPS emission, with levels set at 24.1, 25.05, and 26 MJy sr^{-1}. Top right: ROSAT full-band 0.1–2.4 keV image of the same region, with Spitzer MIPS contours superimposed. The color bar shows a range of 0.6–2.5 smoothed counts on a square-root scale with a Gaussian smoothing, see Appendix B. Bottom: Swift-XRT hard-band 2–10 keV and soft-band 0.3–2.0 keV images of the same region (left and right, respectively), smoothed with a boxcar kernel, see Appendix B. Spitzer MIPS contours are superimposed in white for reference. The color bar shows a range of 0–0.05 smoothed counts on a linear scale.

[11] https://www.swift.ac.uk/LSXPS/

Appendix C
IRAC–2MASS Color Cuts

We utilize the criteria presented in Gutermuth et al. (2009) and Winston et al. (2019) to select YSO candidates in DC 314.8–5.1 based on Spitzer IRAC mapping data, as outlined in Section 3.2. The top left panel of Figure 7 displays the full extent of the Spitzer sample in the region, in which 1319 sources are detected within 5′ of the center of DC 314.8–5.1, as well as the first selection cut to remove star-forming galaxies. Figure 7 further displays the selections done on the sample to remove contaminating sources, beginning with the removal of star-forming galaxies (top panels), then AGNs, and finally unresolved PAH and shock emission (bottom left and right panels, respectively). We further show the final selection, identifying Class I and Class II YSOs, in Figure 8. Sources that fall outside the YSO selection regions (923 sources) are unidentified in the selection and assumed to fall under the Class III or field star category. Given that these remaining sources are heavily contaminated with AGB stars in similar samples (see Dunham et al. 2015), we further cross-correlated with Gaia-measured distances and further discussed them in Sections 3.3 and 4.

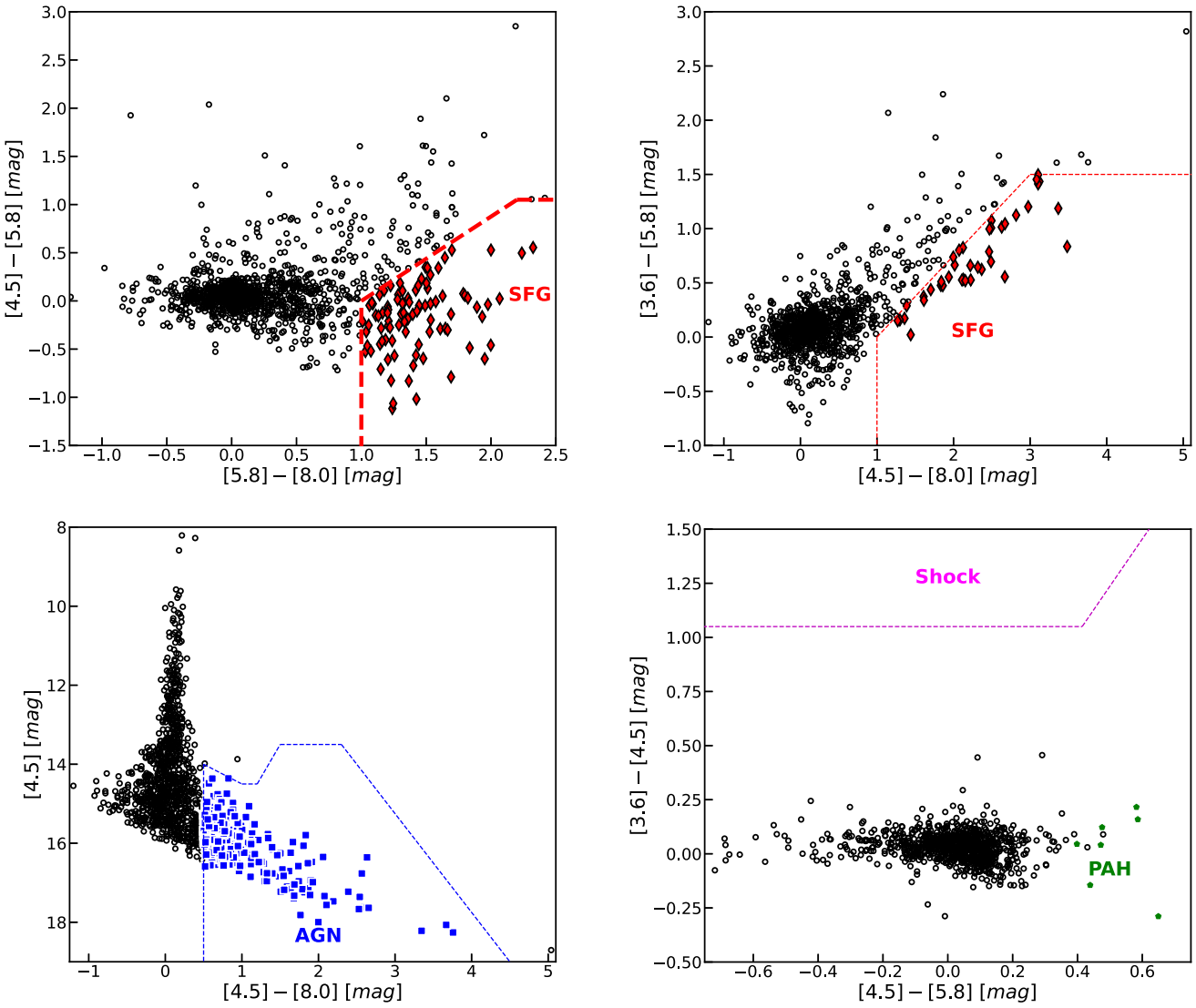

Figure 7. IRAC color–color diagram with selection cuts from Gutermuth et al. (2009). Top left: a total of 1319 sources from the SEIP query of 5′ radius from the optical center of DC 314.8–5.1. It is overlaid with the first selection cut, red dashed lines showing the removal of star-forming galaxies (SFG). Top right: second SFG selection cut; removed sources are marked as red diamonds. Bottom left: AGN selection cut with AGN-like sources marked in blue. Bottom right: selection cut in order to remove Galactic-scale unresolved shocks and unresolved sources of PAH emission; sources of PAH emission are marked with green pentagons; no unresolved shock sources were selected.

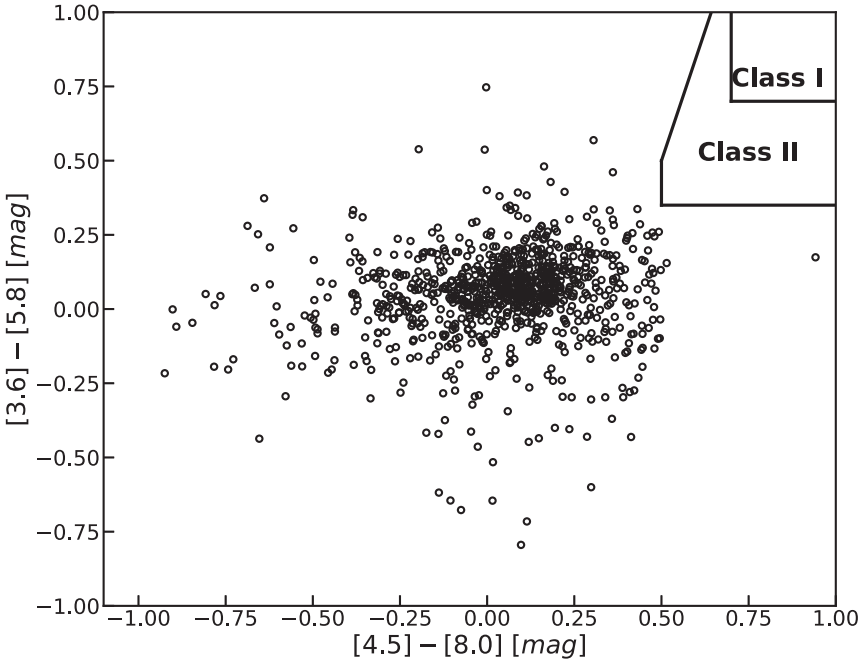

Figure 8. IRAC color–color diagram with YSO selection criteria from Gutermuth et al. (2009). The black marked regions display the final selection cuts identifying YSO Class I and II sources. Sources outside the delineated regions are undefined in this selection.

ORCID iDs

E. Kosmaczewski https://orcid.org/0000-0001-7150-4706
Ł Stawarz https://orcid.org/0000-0002-7263-7540
C. C. Cheung https://orcid.org/0000-0002-4377-0174
A. Bamba https://orcid.org/0000-0003-0890-4920
A. Karska https://orcid.org/0000-0001-8913-925X
W. R. M. Rocha https://orcid.org/0000-0001-6144-4113

References

Ackermann, M., Ajello, M., Baldini, L., et al. 2018, ApJS, 237, 32
Anderson, A. R., Williams, J. P., van der Marel, N., et al. 2022, ApJ, 938, 55
André, P., Di Francesco, J., Ward-Thompson, D., et al. 2014, in Protostars and Planets VI, ed. H. Beuther (Tucson, AZ: Univ. of Arizona Press), 27
Bailer-Jones, C. A. L., Rybizki, J., Fouesneau, M., Demleitner, M., & Andrae, R. 2021, AJ, 161, 147
Bamba, A., Yamazaki, R., Kohri, K., et al. 2009, ApJ, 691, 1854
Barsony, M. 1997, CoKon, 100, 189
Beckwith, S. V. W., Sargent, A. I., Chini, R. S., et al. 1990, AJ, 99, 924
Beichman, C. A., Neugebauer, G., Habing, H. J., Clegg, P. E., & Chester, T. J. 1988, IRAS Catalogs and Atlases, 1: Explanatory Supplement
Bergin, E. A., & Tafalla, M. 2007, ARA&A, 45, 339
Boller, T., Freyberg, M. J., Trümper, J., et al. 2016, A&A, 588, A103
Bourke, T. L., Hyland, A. R., Robinson, G., et al. 1995a, MNRAS, 276, 1052
Bourke, T. L., Hyland, A. R., Robinson, G., et al. 1995b, MNRAS, 276, 1067
Burrows, D. N., Hill, J. E., Nousek, J. A., et al. 2000, Proc. SPIE, 4140, 64
Cardelli, J. A., Clayton, G. C., & Mathis, J. S. 1989, ApJ, 345, 245
Connelley, M. S., Reipurth, B., & Tokunaga, A. T. 2007, AJ, 133, 1528
D'Alessio, P., Calvet, N., & Hartmann, L. 2001, ApJ, 553, 321
Dunham, M. M., Allen, L. E., Evans, N. J., et al. 2015, ApJS, 220, 11
Dunham, M. M., & Vorobyov, E. I. 2012, ApJ, 747, 52
Evans, N. J. I., Dunham, M. M., & Jørgensen, J. K. 2009, ApJS, 181, 321
Evans, P. A., Osborne, J. P., Beardmore, A. P., et al. 2014, ApJS, 210, 8
Evans, P. A., Page, K. L., Osborne, J. P., et al. 2020, ApJS, 247, 54
Fazio, G. G., Hora, J. L., Allen, L. E., et al. 2004, ApJS, 154, 10
Gabici, S. 2013, in Astrophysics and Space Science Proc. 34, San Cugat Forum on Astrophysics, Cosmic Rays in Star-Forming Environments, ed. D. F. Torres & O. Reimer (Berlin: Springer), 221
Gaia Collaboration, Brown, A. G. A., Vallenari, A., et al. 2021, A&A, 649, A1
Gehrels, N. 1986, ApJ, 303, 336
Getman, K. V., & Feigelson, E. D. 2021, ApJ, 916, 32
Getman, K. V., Feigelson, E. D., Garmire, G. P., et al. 2022, ApJ, 935, 43
Greene, T. P., Wilking, B. A., Andre, P., Young, E. T., & Lada, C. J. 1994, ApJ, 434, 614
Grosso, N., Montmerle, T., Bontemps, S., André, P., & Feigelson, E. D. 2000, A&A, 359, 113
Güdel, M., & Nazé, Y. 2009, A&ARv, 17, 309
Gutermuth, R. A., Megeath, S. T., Myers, P. C., et al. 2009, ApJS, 184, 18
Hartley, M., Manchester, R. N., Smith, R. M., Tritton, S. B., & Goss, W. M. 1986, A&AS, 63, 27
Hetem, J. C. G., Sanzovo, G. C., & Lépine, J. R. D. 1988, A&AS, 76, 347
Heyer, M., Dame, T. M., & Dame, A. R. A. 2015, ARA&A, 53, 583
HI4PI Collaboration, Ben Bekhti, N., Flöer, L., et al. 2016, A&A, 594, A116
Høg, E., Fabricius, C., Makarov, V. V., et al. 2000, A&A, 355, L27
Houck, J. R., Roellig, T. L., Van Cleve, J., et al. 2004, Proc. SPIE, 5487, 62
Jørgensen, J. K., Belloche, A., Belloche, A., & Garrod, R. T. 2020, ARA&A, 58, 727
Joye, W. A., & Mandel, E. 2003, in ASP Conf. Ser. 295, Astronomical Data Analysis Software and Systems XII, ed. H. E. Payne, R. I. Jedrzejewski, & R. N. Hook (San Francisco, CA: ASP), 489
Karska, A., Kaufman, M. J., Kristensen, L. E., et al. 2018, ApJS, 235, 30
Kirk, J. M., Ward-Thompson, D., & André, P. 2005, MNRAS, 360, 1506
Klessen, R. S., & Glover, S. C. O. 2016, SAAS, 43, 85
Kosmaczewski, E., Stawarz, L., Rocha, W. R. M., Shenoy, S. S., & Karska, A. 2022, ApJ, 934, 94
Kuhn, M. A., Getman, K. V., Feigelson, E. D., et al. 2010, ApJ, 725, 2485
Lada, C. J. 1987, in IAU Symp. 115, Star Forming Regions, ed. M. Peimbert & J. Jugaku (Dordrecht: Reidel), 1
Makovoz, D., Khan, I., & Moshir, M. 2005, PASP, 117, 274
Mizuno, T., Hayashi, K., Metzger, J., et al. 2022, ApJ, 935, 97
Montmerle, T., Grosso, N., Tsuboi, Y., & Koyama, K. 2000, ApJ, 532, 1097
Planck Collaboration, Ade, P. A. R., Aghanim, N., et al. 2011, A&A, 536, A23
Planck Collaboration, Ade, P. A. R., Aghanim, N., et al. 2016a, A&A, 594, A28
Planck Collaboration, Ade, P. A. R., Aghanim, N., et al. 2016b, A&A, 594, A26
Preibisch, T., & Feigelson, E. D. 2005, ApJS, 160, 390
Rieke, G. H., Young, E. T., Engelbracht, C. W., et al. 2004, ApJS, 154, 25
Roming, P. W. A., Kennedy, T. E., Mason, K. O., et al. 2005, SSRv, 120, 95

Skrutskie, M. F., Cutri, R. M., Stiening, R., et al. 2006, AJ, 131, 1163
Smith, R. K., Brickhouse, N. S., Liedahl, D. A., & Raymond, J. C. 2001, ApJL, 556, L91
Sofue, Y., & Kataoka, J. 2016, PASJ, 68, L8
Stauffer, J. R., Caillault, J. P., Gagne, M., et al. 1994, ApJS, 91, 625
Strom, S. E., Strom, K. M., & Grasdalen, G. L. 1975, ARA&A, 13, 187
van den Bergh, S., & Herbst, W. 1975, AJ, 80, 208
Vilhu, O., & Walter, F. M. 1987, ApJ, 321, 958
Wang, J., Feigelson, E. D., Townsley, L. K., et al. 2009, ApJ, 696, 47
Whittet, D. C. B. 2007, AJ, 133, 622
Winston, E., Hora, J., Gutermuth, R., & Tolls, V. 2019, ApJ, 880, 9
Wright, E. L., Eisenhardt, P. R. M., Mainzer, A. K., et al. 2010, AJ, 140, 1868